Exceptional synergistic enhancement of the photocatalytic activity of SnS$_2$ by coupling with polyaniline and N-doped reduced graphene oxide

Fen Zhang[a], Yongcai Zhang[a,*], Geshan Zhang[b], Zhanjun Yang[a], Dionysios D. Dionysiou[c], Aiping Zhu[a,*]

[a] School of Chemistry and Chemical Engineering, Yangzhou University, Yangzhou 225009, China
[b] College of Chemical Engineering, Zhejiang University of Technology, Hangzhou 310014, China
[c] Environmental Engineering and Science Program, Department of Chemical and Environmental Engineering, University of Cincinnati, Cincinnati, OH, 45221-0012, USA

ARTICLE INFO

ABSTRACT

Effective enhancement of the separation and transfer of photogenerated electrons and holes of semiconductor photocatalysts is key to increase their photocatalytic efficiency. This study aims at improving the photocatalytic performance of visible-light-responsive, CdI$_2$-type layered SnS$_2$ by employing good conductivity N-doped reduced graphene oxide (NRG) and polyaniline (PANI) as the receptors and transporters of photogenerated electrons and holes, respectively. PANI/SnS$_2$/NRG ternary composites were prepared by a three-step method, and the optimum conditions for preparing the most efficient product were explored. The photocatalytic experiments demonstrated that the PANI/SnS$_2$/NRG ternary composite prepared under the optimum conditions (PANI/SnS$_2$/NRG-2%) had markedly higher photocatalytic activity than SnS$_2$ nanoplates, SnS$_2$/PANI and SnS$_2$/NRG binary composites in the reduction of aqueous Cr(VI) under the irradiation of visible-light ($\lambda > 420$ nm). Based on comparison of the photoabsorption, photoluminescence and electrochemical impedance properties of PANI/SnS$_2$/NRG, SnS$_2$/PANI and SnS$_2$, it was thought that the coupling of SnS$_2$ with both PANI and NRG had synergistic effects in increasing the absorption of visible-light as well as the separation and transfer of photogenerated electrons and holes, which contributed to the exceptionally high photocatalytic activity of PANI/SnS$_2$/NRG ternary composite. Moreover, it was discovered that the photocatalytic reduction of Cr(VI) over PANI/SnS$_2$/NRG-2% was dominantly through the reduction by photogenerated electrons, whereas both photogenerated electron and superoxide anion radical (O$_2\cdot^-$) reduction played important roles in the photocatalytic reduction of Cr(VI) over SnS$_2$. Besides, the influences of photocatalytic testing conditions (including starting pH and concentration of Cr(VI) solution, and dosage of photocatalyst) on the efficiency of PANI/SnS$_2$/NRG-2% in treatment of aqueous Cr(VI) were also examined.

1. Introduction

Cr(VI) commonly exists in the wastewaters generated by chromate manufacturing, electroplating, metallurgy, and leather tanning industries, etc. It is highly toxic and mobile, so it has been commonly categorized as a precedence-controlled pollutant. The toxicity and mobility can be greatly lowered once Cr(VI) is reduced to Cr(III) [1–8]. In comparison with conventional chemical reduction methods, photocatalytic reduction has the distinct advantages of more environmental benefit and lower cost, so it is more promising for industrial application [1–8]. However, most photocatalysts synthesized to date have relatively low photocatalytic activity in the reduction of Cr(VI) under the irradiation of visible-light (nearly 43% of natural sunlight energy) [9]. Therefore, for effective utilization of clean, free and inexhaustible

sunlight energy in photocatalytic treatment of Cr(VI)-contaminated water, it is imperative to develop new efficient visible-light-driven photocatalysts.

Layered semiconductors are good candidate materials for making photocatalysts, because their intrinsic layered structure facilitates the separation and transportation of photogenerated electrons (e^-) and holes (h^+) [10–15]. Moreover, layered semiconductors are prone to form two-dimensional nanostructures, which not only have large specific surface areas with more active sites, but also are excellent units for assembling heterojunctions [10–15]. SnS$_2$ is an inexpensive, nontoxic, and visible-light-responsive semiconductor (E$_g$ = 2.2 eV) with a CdI$_2$-type layered structure [16]. SnS$_2$ holds great potential for use as a new sunlight-driven photocatalyst, because it has not only significant visible-light-activated photocatalytic activity for a variety of chemical

---

reactions [16–21], etc., but also relatively good photocatalytic stability [16–20]. Nevertheless, SnS_2 also has the shortcoming of relatively low photocatalytic efficiency due to the fast recombination and slow transfer of its e^- and h^+. Among the modification methods proposed for increasing the photocatalytic efficiency of SnS_2, construction of heterojunctions turned out to be fairly effective [22–37]. Until now, a number of materials including SnO_2 [22], TiO_2 [23], g-C_3N_4 [24], $La_2Ti_2O_7$ [25], Bi_2S_3 [26], SnS [27], Ag_3PO_4 [28], Ag_2CrO_4 [29], CeO_2 [30], Ag_2S [31], BiOBr [32], carbon nanofibers [33], graphene [34–36], and PANI [37], etc. have been tried to combine with SnS_2 to form heterojunctions. These heterojunctions can all enhance the separation of e^--h^+ pairs of SnS_2 to a certain degree, resulting in higher photocatalytic efficiency. Particularly, modification of SnS_2 by combination with good conductivity graphene and PANI has demonstrated considerable enhancement of photocatalytic activity [34–37].

Graphene and its derivatives (such as reduced graphene oxide (RGO)) have been actively explored as an effective cocatalyst for constructing composite photocatalysts, mainly owing to their high electron mobility and high specific surface area [34–36,38–41]. For example, H. Chauhan, et al. synthesized RGO-stacked SnS_2 nanodiscs, which exhibited much higher photocatalytic activity than SnS_2 nanodiscs in synthesizing aniline from nitrobenzene, reducing Cr(VI) and degrading dyes under visible-light irradiation [34]. Y. Yuan, et al. prepared a composite photocatalyst comprising SnS_2 quantum dots on RGO, which exhibited higher efficiency than SnS_2 quantum dots in visible-light-driven photocatalytic reduction of Cr(VI) [35]. P. Chen, et al. prepared RGO nanosheet-supported interconnected SnS_2 nanosheets, which demonstrated more efficient visible-light-driven photocatalytic degradation of phenol and rhodamine B as compared with SnS_2 nanosheets [36]. In the reported SnS_2/RGO composite photocatalysts, RGO functioned as the acceptor and transporter of e^- of SnS_2 under visible-light excitation [34–36]. Thus, the coupling of SnS_2 with RGO can suppress the recombination of e^--h^+ pairs, leading to enhancement of photocatalytic activity.

PANI is an extensively studied conducting polymer having the advantages of high conductivity, low cost, nontoxicity and good environmental stability [37,42–47]. It presents many outstanding features for use as a modifier in improving the photocatalytic performance of inorganic semiconductors [37,42–47], including: (i) good charge-transporting ability, thus facilitating the transfer and separation of e^- and h^+; (ii) excellent visible-light-absorbing ability, thus acting as a photosensitizer or photogenerated electron donor; and (iii) matched band structure to form heterojunction with inorganic semiconductors, thus contributing to efficient interfacial charge transfer. As a result, the combination with PANI turned out to be highly effective in improvement of the photocatalytic performance of inorganic semiconductors [37,42–47]. For example, our previous work has shown that PANI/SnS_2 composite had remarkably higher visible-light-driven photocatalytic activity than pristine SnS_2 in the reduction of Cr(VI) [37]. We ascribed the higher visible-light-driven photocatalytic activity of SnS_2/PANI composite to its increased Cr(VI) adsorption, enhanced visible-light absorption, as well as more efficient separation and transfer of e^- and h^+ owing to the formation of type-II heterojunction between SnS_2 and PANI [37].

Previous works have reported that coupling with either RGO or PANI can dramatically enhance the photocatalytic activity of SnS_2 [34–37]. In SnS_2/RGO heterojunction, RGO acts as the receptor and transporter of the photogenerated electrons of SnS_2 [34–36]; whereas in SnS_2/PANI heterojunction, PANI functions as the receptor and transporter of photogenerated holes as well as the photogenerated electron donor [37]. The good conductivity of RGO and PANI can facilitate the transfer and separation of e^- and h^+ of SnS_2, resulting in increased photocatalytic efficiency. Therefore, if SnS_2, RGO and PANI are rationally integrated into a ternary composite, PANI/SnS_2/RGO, there would be synergistic effects of SnS_2/RGO and SnS_2/PANI heterojunctions for photocatalytic enhancement. Moreover, for the PANI/SnS_2/ RGO ternary composite, the reduction and oxidation reactions would occur on RGO and PANI, respectively, which can inhibit the photocorrosion of SnS_2 [48–50]. Thus, it would be expected that the photocatalytic performance of PANI/SnS_2/RGO ternary composite would surpass those of binary SnS_2/RGO and SnS_2/PANI. Besides, N-doped reduced graphene oxide (NRG) not only retains the advantageous properties of RGO, but also gains additional favorable properties such as increased electrical conductivity for faster electron transfer [51–53]. Hence, in this study, we attempted to prepare a new PANI/SnS_2/NRG ternary composite photocatalyst, and investigated its photocatalytic properties in the reduction of aqueous Cr(VI) under the irradiation of visible-light ($\lambda > 420$ nm). The optimum synthesis conditions of PANI/SnS_2/NRG composite photocatalyst were explored for obtaining the most efficient product. The composition, structure, optical and electrochemical impedance properties of the as-prepared PANI/SnS_2/NRG composites were characterized. Moreover, the mechanisms of photocatalytic reduction of Cr(VI) by PANI/SnS_2/NRG composite and SnS_2 were investigated. Besides, the influences of photocatalytic testing conditions (including starting pH and concentration of Cr(VI) solution, and dosage of photocatalyst) on the efficiency of PANI/SnS_2/NRG-2% in treatment of aqueous Cr(VI) were also examined.

2. Experimental

2.1. Preparation of PANI/SnS₂/NRG ternary composites

PANI/SnS_2/NRG ternary composites were synthesized via the following three steps:

(1) SnS_2 nanoplates were prepared through hydrothermal reactions of $SnCl_4 \cdot 5H_2O$ (6 mmol) and thioacetamide (15 mmol) in 40 mL of aqueous solution at 190 °C for 13 h;

(2) A series of SnS_2/PANI nanocomposites were prepared via first mixing of 1000 mg SnS_2 nanoplates and different amounts (50, 70 or 90 mg) of PANI (molecular weight: 50,000–60,000; electric conductivity: 2 s/cm) in 20 mL of N,N-Dimethylformamide by ultrasonic dispersion for 30 min and magnetic stirring for 3 h, then, evaporation of N,N-Dimethylformamide by heating at 140 °C for 12 h. The resulting SnS_2/PANI nanocomposites were labeled as SnS_2/PANI-5%, SnS_2/PANI-7% and SnS_2/PANI-9%, respectively, according to the mass ratios of PANI to SnS_2 nanoplates;

(3) A series of PANI/SnS_2/NRG ternary composites were synthesized via hydrothermal treatment of 1000 mg SnS_2/PANI-7% and different amounts (10, 20 or 30 mg) of graphene oxide in the mixed solvent of 38.0 mL of deionized water and 2.0 mL of hydrazine hydrate (85 mass%) at 120 °C for 6 h. The as-synthesized PANI/ SnS_2/NRG ternary composites were labeled as PANI/SnS_2/NRG-1%, PANI/SnS_2/NRG-2% and PANI/SnS_2/NRG-3%, respectively, according to the mass ratios of graphene oxide to SnS_2/PANI-7% used.

2.2. Characterization and photocatalytic evaluation of the products

The information on the characterization and photocatalytic evaluation of the products was provided in the Supplementary Material.

3. Results and discussion

3.1. Optimization of the preparation conditions of PANI/SnS₂/NRG composite

Fig. 1 shows the Cr(VI) adsorption and photocatalytic reduction performance of SnS_2 nanoplates, and SnS_2/PANI nanocomposites prepared using different mass ratios of PANI to SnS_2 nanoplates. As can be noticed from Fig. 1, SnS_2/PANI-5%, SnS_2/PANI-7% and SnS_2/PANI-9% all exhibited obviously more adsorption as well as accelerated photocatalytic reduction of Cr(VI) in comparison with SnS_2 nanoplates. In
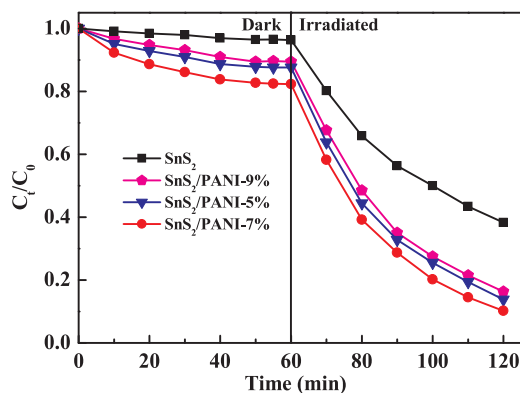
Fig. 1. Cr(VI) adsorption and photocatalytic reduction performance of SnS_2 nanoplates, and SnS_2/PANI nanocomposites prepared using different mass ratios of PANI to SnS_2 nanoplates.

Fig. 2. Cr(VI) adsorption and photocatalytic reduction performance of SnS_2 nanoplates, SnS_2/PANI-7%, SnS_2/NRG-2%, and PANI/SnS_2/NRG ternary composites synthesized using different mass ratios of graphene oxide to SnS_2/PANI-7%.

addition, the mass ratios of PANI to SnS_2 in SnS_2/PANI nanocomposites affected their Cr(VI) adsorption and photocatalytic reduction performance. The equilibrium Cr(VI) adsorption amounts by SnS_2/PANI-5%, SnS_2/PANI-7%, SnS_2/PANI-9% and SnS_2 nanoplates were about 12%, 18%, 11% and 4%, respectively. Clearly, SnS_2/PANI-7% demonstrated the largest adsorption capacity for Cr(VI). For quantitatively comparing the photocatalytic activities of SnS_2 nanoplates, SnS_2/PANI-5%, SnS_2/PANI-7% and SnS_2/PANI-9%, the reaction rate constant (k) for each sample-mediated photocatalytic reduction of Cr(VI) was estimated adopting the pseudo-first order kinetic model as expressed by Eq. (1) [54–57]:

$$\ln(C_{i0}/C_{it}) = kt \tag{1}$$

In Eq. (1), C_{i0} and C_{it} denote in turn the Cr(VI) concentration just after 60 min dark adsorption and just after t min visible-light irradiation. The plots of $\ln(C_{i0}/C_{it})$ versus t in the case of using SnS_2/PANI-5%, SnS_2/PANI-7%, SnS_2/PANI-9% and SnS_2 nanoplates as photocatalyst are provided in Fig. S1, from which we can obtain the k and correlation coefficient (R^2) values as listed in Table 1. Apparently, the values of R^2 in all the cases were all near 1, implying that first order reaction kinetics can be applicable to the photocatalytic reduction of Cr(VI) over SnS_2/PANI-5%, SnS_2/PANI-7%, SnS_2/PANI-9% and SnS_2 nanoplates. The values of k in the presence of different samples were in the order of SnS_2/PANI-7% > SnS_2/PANI-5% > SnS_2/PANI-9% > SnS_2 nanoplates. Obviously, SnS_2/PANI-7% had the highest photocatalytic activity. Therefore, SnS_2/PANI-7% was used later for synthesis of PANI/SnS_2/NRG ternary composites.

Fig. 3. XRD patterns of (a) SnS_2, (b) SnS_2/PANI-7% and (c) PANI/SnS_2/NRG-2%.
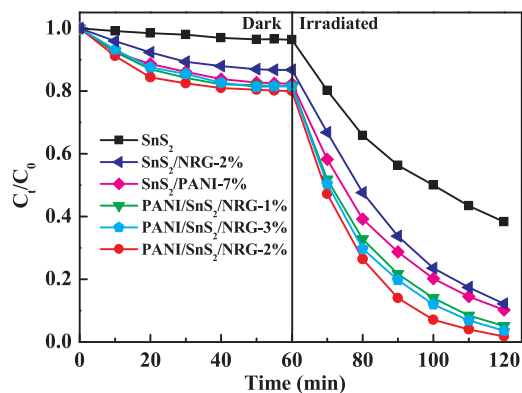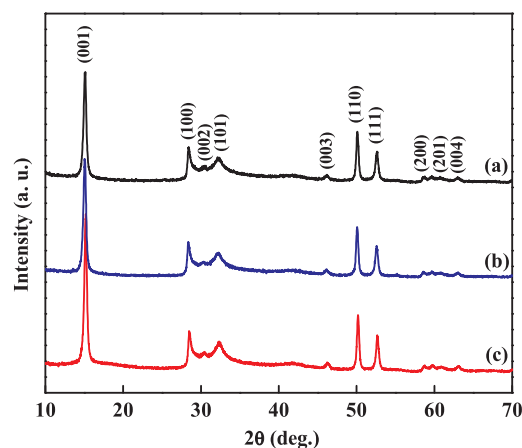
Fig. 2 shows the Cr(VI) adsorption and photocatalytic reduction performance of SnS_2 nanoplates, SnS_2/PANI-7%, SnS_2/NRG-2%, and PANI/SnS_2/NRG ternary composites synthesized using different mass ratios of graphene oxide to SnS_2/PANI-7%. It can be observed from Fig. 2 that compared with SnS_2/PANI-7%, SnS_2/NRG-2% and SnS_2 nanoplates, PANI/SnS_2/NRG ternary composites demonstrated a little more adsorption and noticeably faster photocatalytic reduction of Cr
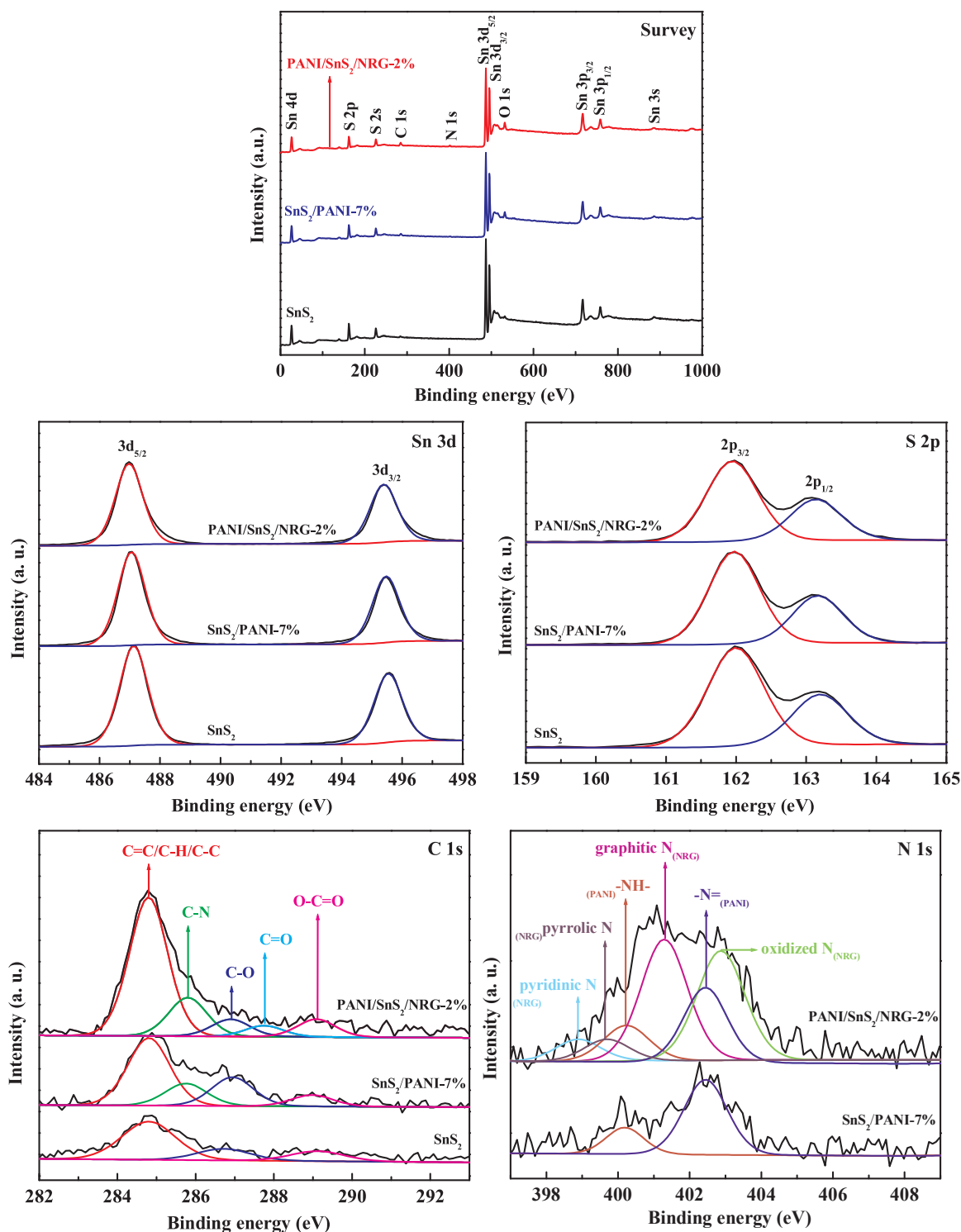
Table 1

The k and R^2 values for photocatalytic reduction of Cr(VI) by different samples under various experimental conditions.

Sample	Dosage (mg)	$C(K_2Cr_2O_7)$ (mg/L)	pH of $K_2Cr_2O_7$ solution	K (min^{-1})	R^2
SnS_2	300	50	5.3	0.016	0.991
SnS_2/PANI-5%	300	50	5.3	0.031	0.997
SnS_2/PANI-7%	300	50	5.3	0.035	0.999
SnS_2/PANI-9%	300	50	5.3	0.029	0.997
SnS_2/NRG-2%	300	50	5.3	0.033	0.999
PANI/SnS_2/NRG-1%	300	50	5.3	0.045	0.999
PANI/SnS_2/NRG-2%	300	50	5.3	0.061	0.998
PANI/SnS_2/NRG-3%	300	50	5.3	0.050	0.997
PANI/SnS_2/NRG-2%	100	50	5.3	0.018	0.989
PANI/SnS_2/NRG-2%	200	50	5.3	0.027	0.989
PANI/SnS_2/NRG-2%	400	50	5.3	0.105	0.997
PANI/SnS_2/NRG-2%	300	50	3.0	0.132	0.996
PANI/SnS_2/NRG-2%	300	50	7.0	0.020	0.996
PANI/SnS_2/NRG-2%	300	50	9.0	0.009	0.996
PANI/SnS_2/NRG-2%	300	25	5.3	0.176	0.997
PANI/SnS_2/NRG-2%	300	75	5.3	0.028	0.999
PANI/SnS_2/NRG-2%	300	100	5.3	0.021	0.999

Fig. 4. XPS spectra of SnS_2, SnS_2/PANI-7% and PANI/SnS_2/NRG-2%.

(VI). Through the plots of $\ln(C_{i0}/C_{it})$ versus t as shown in Fig. S2, the values of k for visible-light ($\lambda > 420$ nm)-driven photocatalytic reduction of Cr(VI) over PANI/SnS_2/NRG-1%, PANI/SnS_2/NRG-2%, PANI/SnS_2/NRG-3%, SnS_2/PANI-7%, SnS_2/NRG-2% and SnS_2 nanoplates were obtained as presented in Table 1. It can be identified from Table 1 that PANI/SnS_2/NRG-2% exhibited the highest photocatalytic efficiency among all the samples. This suggested that the optimal mass ratio of graphene oxide to SnS_2/PANI-7% for preparation of PANI/SnS_2/NRG ternary composite was 2%. The photocatalytic activity of PANI/SnS_2/NRG-2% ($k = 0.061$ min^{-1}) was about 3.8 times that of

SnS_2 nanoplates ($k = 0.016$ min^{-1}).

3.2. Characterization of the composition and structure of PANI/SnS_2/NRG composite

The XRD patterns of the as-prepared SnS_2, SnS_2/PANI-7% and PANI/SnS_2/NRG-2% are shown in Fig. 3(a–c), respectively. As indicated in Fig. 3(a), the XRD peaks of the hydrothermally synthesized SnS_2 can all be indexed to the hexagonal phase tin disulfide (JCPDS File No. 23-677). SnS_2/PANI-7% and PANI/SnS_2/NRG-2% displayed similar
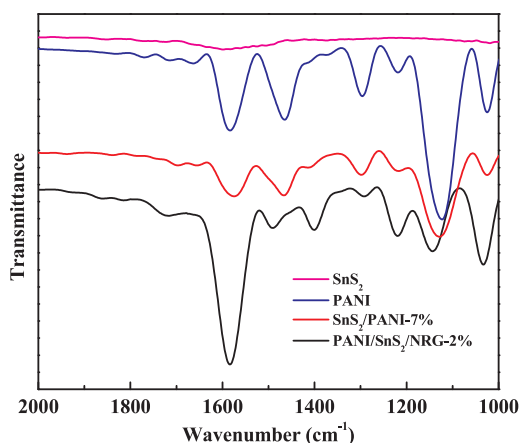
Fig. 5. FTIR spectra of SnS$_2$, PANI, SnS$_2$/PANI-7% and PANI/SnS$_2$/NRG-2%.

XRD patterns as SnS$_2$. No XRD peaks of PANI and NRG can be seen in the XRD spectrum (Fig. 3(c)) of PANI/SnS$_2$/NRG-2%. This was probably due to the relatively low proportion of PANI and NRG in PANI/SnS$_2$/NRG-2%. However, the incorporation of PANI and NRG into PANI/SnS$_2$/NRG-2% was confirmed by further XPS, FTIR and TEM characterizations.

The surface elemental compositions and chemical valences of SnS$_2$, SnS$_2$/PANI-7% and PANI/SnS$_2$/NRG-2% were measured employing XPS, and the obtained results are illustrated in Fig. 4. The survey XPS spectra revealed that except for adventitious C and O, SnS$_2$ contained

Sn and S, SnS$_2$/PANI-7% contained Sn, S, C and N, whereas PANI/SnS$_2$/NRG-2% contained Sn, S, C, N and O. The surface C and N contents (atomic%) in SnS$_2$/PANI-7% were about 15.3% and 3.4%, respectively, whereas those in PANI/SnS$_2$/NRG-2% were about 21.8% and 6.0%, respectively. This was also in agreement with the EDX analysis results that PANI/SnS$_2$/NRG-2% had more C content than SnS$_2$/PANI-7% (Fig. S3). The Sn 3d XPS spectra of SnS$_2$, SnS$_2$/PANI-7% and PANI/SnS$_2$/NRG-2% displayed two peaks belonging to Sn 3d$_{3/2}$ and Sn 3d$_{5/2}$, respectively. The binding energies of Sn 3d$_{5/2}$ of SnS$_2$, SnS$_2$/PANI-7% and PANI/SnS$_2$/NRG-2% were about 487.0–487.1 eV, which can be assigned to Sn^{4+} [58–60]. The S 2p XPS spectra of SnS$_2$, SnS$_2$/PANI-7% and PANI/SnS$_2$/NRG-2% displayed two peaks corresponding to S 2p$_{1/2}$ and S 2p$_{3/2}$, respectively. The binding energies of S 2p$_{3/2}$ of SnS$_2$, SnS$_2$/PANI-7% and PANI/SnS$_2$/NRG-2% were all nearly 162.0 eV, which was in accord with S^{2-} [58–60]. The C 1s XPS spectrum of SnS$_2$ was fitted into three peaks at about 284.8, 286.7, and 289.1 eV, which may arise from the adsorbed C=C/C−H/C−C, C−O, and O−C=O [60], respectively. The C 1s XPS spectrum of SnS$_2$/PANI-7% was fitted into four peaks at about 284.8, 285.8, 286.9, and 289.1 eV, which may be attributed to C=C/C−H/C−C, C−N, C−O, and O−C=O [60–63], respectively. By contrast, the C 1s XPS spectrum of PANI/SnS$_2$/NRG-2% was fitted into five peaks at about 284.8, 285.8, 286.9, 287.8, and 289.1 eV, which in sequence can be ascribed to C=C/C−H/C−C, C−N, C−O, C=O, and O−C=O [60–63]. The N 1s XPS spectrum of SnS$_2$/PANI-7% was fitted into two peaks at about 400.2 and 402.4 eV, which in turn can be attributed to −NH− and −N= of PANI [64,65]. However, the N 1s XPS spectrum of PANI/SnS$_2$/NRG-2% can be fitted into six peaks at about 398.9, 399.7, 400.2, 401.3, 402.4, and 402.8 eV,
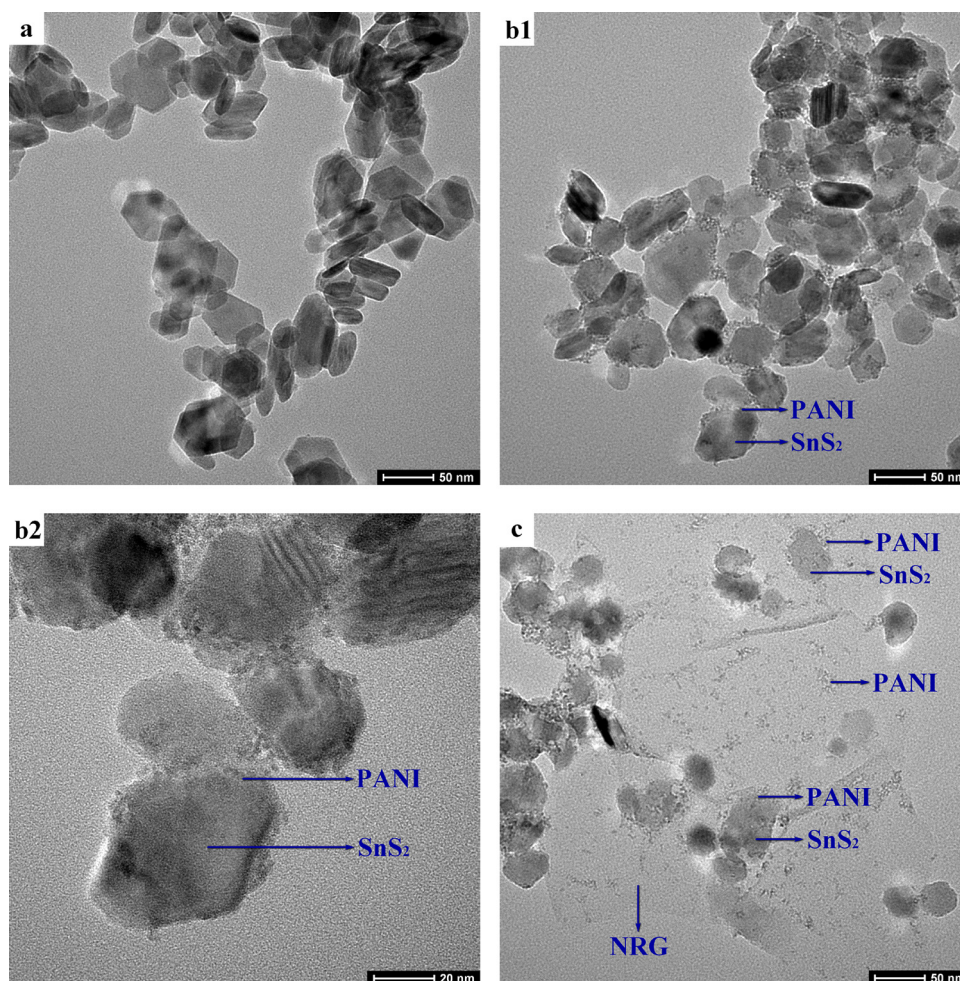

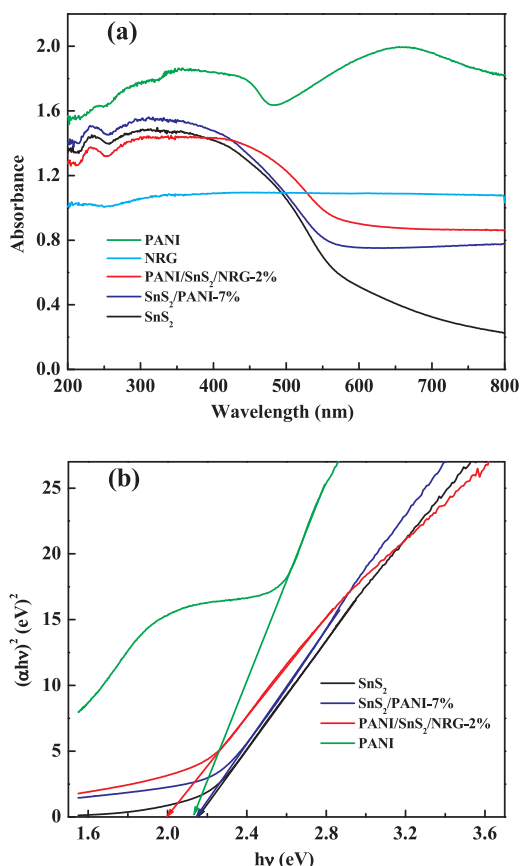**Fig. 6.** TEM images of (a) SnS$_2$, (b1 and b2) SnS$_2$/PANI-7% and (c) PANI/SnS$_2$/NRG-2%.

Fig. 7. (a) UV–vis absorption spectra of PANI, NRG, SnS$_2$, SnS$_2$/PANI-7% and PANI/SnS$_2$/NRG-2%, which were transformed from their UV–vis diffuse reflectance spectra using the Kubelka-Munk function; **(b)** Plots of $(\alpha h\nu)^2$ vs. (hν) for estimation of the E$_g$ values of PANI, SnS$_2$, SnS$_2$/PANI-7% and PANI/SnS$_2$/NRG-2%.
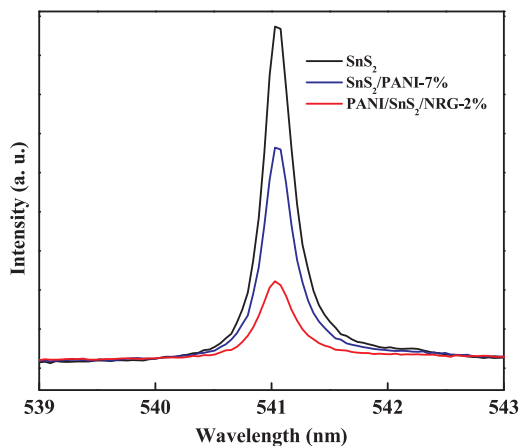

Fig. 8. Room temperature photoluminescence spectra of SnS$_2$, SnS$_2$/PANI-7% and PANI/SnS$_2$/NRG-2% upon 532 nm laser excitation.

which may be assigned to pyridinic N (NRG), pyrrolic N (NRG), −NH− (PANI), graphitic N (NRG), −N= (PANI), and pyridinic N oxide (NRG) [51–53,60–63], respectively. In comparison with SnS$_2$/PANI-7%, the increase of C and N contents as well as the appearance of new C and N species in PANI/SnS$_2$/NRG-2% suggested the existence of NRG in PANI/SnS$_2$/NRG-2%.

The FTIR spectra of SnS$_2$, PANI, SnS$_2$/PANI-7% and PANI/SnS$_2$/NRG-2% in the wavenumber range of 2000–1000 cm^{-1} are presented in Fig. 5. There was no strong peak appearing in the FTIR spectrum of
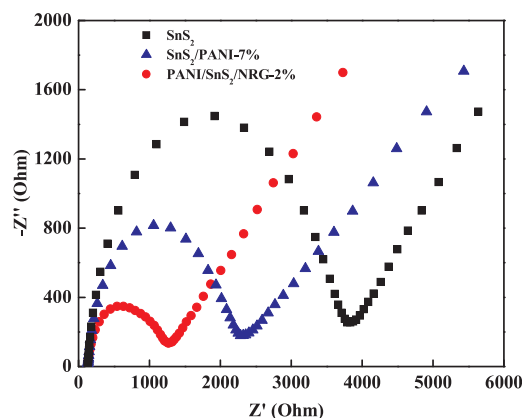

Fig. 9. Electrochemical impedance spectra of SnS$_2$, SnS$_2$/PANI-7% and PANI/SnS$_2$/NRG-2%.

SnS$_2$. The FTIR spectrum of PANI displayed several characteristic peaks at about 1026, 1124, 1220, 1298, 1466, and 1585 cm^{-1}, which could be assigned to ν(sulfo group O=S=O), δ(in plane aromatic C−H), ν(quinoid ring = NH$^+$-benzene ring), ν(benzenoid C−N), ν(benzenoid C=C), and ν(quinoid C=C) [66–70], respectively. The characteristic FTIR peaks of PANI also appeared in the FTIR spectrum of SnS$_2$/PANI-7%, suggesting that SnS$_2$/PANI-7% contained PANI. By comparison with that of SnS$_2$/PANI-7%, the FTIR spectrum of PANI/SnS$_2$/NRG-2% displayed a new peak at about 1725 cm^{-1}, which may stem from the C=O stretching vibration of N-doped reduced graphene oxide [63]. Moreover, the relative intensities of the FTIR peaks of PANI/SnS$_2$/NRG-2% at about 1585, 1220, and 1035 cm^{-1} became exceptionally stronger than those of SnS$_2$/PANI-7%, which may be due to the overlapping of ν(skeleton of graphene), ν(aromatic C−OH), and ν(C−O−C) of NRG with ν(quinonoid C=C), ν(quinoid ring = NH$^+$-benzene ring), and ν(sulfo group O=S=O) of PANI, respectively. The above FTIR information suggested that there was NRG in PANI/SnS$_2$/NRG-2%.

Fig. 6(a), (b1 and b2), and (c) show the TEM images of SnS$_2$, SnS$_2$/PANI-7%, and PANI/SnS$_2$/NRG-2%, respectively. In Fig. 6(a), it can be found that the hydrothermally synthesized SnS$_2$ consisted of nanoplates, which were about 27–50 nm in length/width and 8–20 nm in thickness. The TEM images of SnS$_2$/PANI-7% in Fig. 6(b1 and b2) indicated that the binary composite consisted of SnS$_2$ nanoplates decorated with much smaller (about 2 nm) PANI nanoparticles. Fig. 6(c) revealed that PANI/SnS$_2$/NRG-2% comprised NRG nanosheets loading with SnS$_2$/PANI nanocomposite and PANI nanoparticles. Clearly, in the ternary composite, SnS$_2$/PANI and SnS$_2$/NRG heterojunctions were formed.

3.3. Optical and electrochemical impedance properties of PANI/SnS$_2$/NRG composite

Fig. 7(a) shows the UV–vis absorption spectra of PANI, NRG, SnS$_2$, SnS$_2$/PANI-7% and PANI/SnS$_2$/NRG-2%, which were transformed from their UV–vis diffuse reflectance spectra using the Kubelka-Munk function as expressed by Eqs. (2) and (3) [26,71]:

$$F(R_\infty) = (1 - R_\infty)^2/2R_\infty = \alpha/S \qquad (2)$$

$$R_\infty = R(Sample)/R(BaSO_4) \qquad (3)$$

where $F(R_\infty)$, R, α and S denote in sequence the Kubelka-Munk function, reflectance, absorption coefficient and scattering coefficient. It can be observed from Fig. 7(a) that all the samples demonstrated significant absorption of light in the visible spectrum. Nevertheless, for the light with wavelength longer than 425 nm, the absorption intensities of SnS$_2$ nanoplates, SnS$_2$/PANI-7% and PANI/SnS$_2$/NRG-2% were in an ascending order. The increased visible-light absorption of PANI/SnS$_2$/
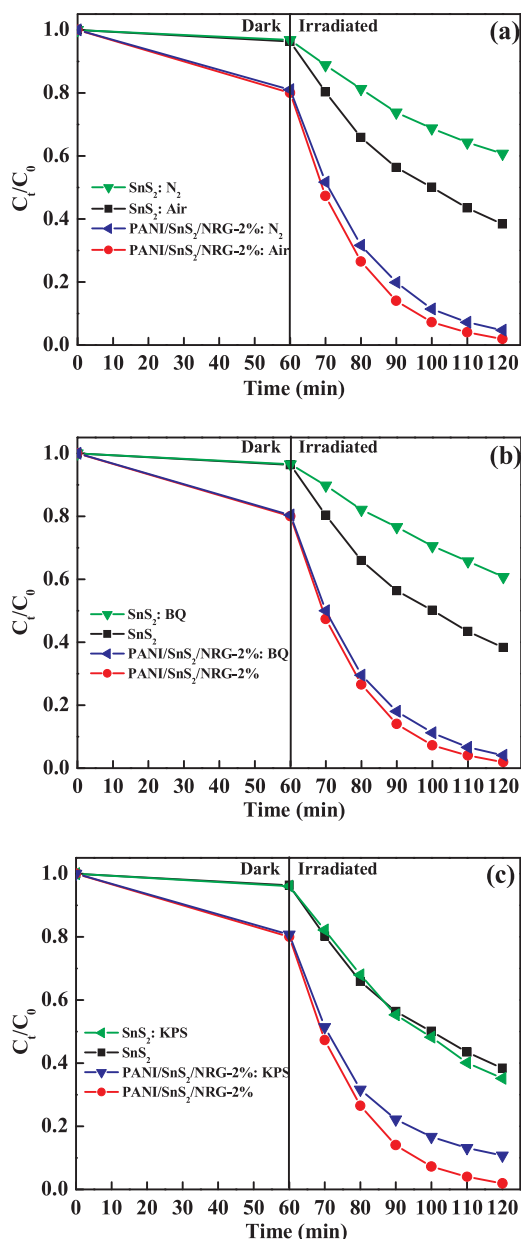
Fig. 10. (a) Photocatalytic reduction of aqueous Cr(VI) by PANI/SnS$_2$/NRG-2% and SnS$_2$ under visible-light (λ > 420 nm) irradiation in N$_2$ or air atmosphere; **(b)** Photocatalytic reduction of aqueous Cr(VI) by PANI/SnS$_2$/NRG-2% and SnS$_2$ under visible-light (λ > 420 nm) irradiation in the presence or absence of superoxide anion radical (O$_2$·$^-$) scavenger (p-Benzoquinone, BQ); *Note*: the dosage of BQ was 1 mL of 0.306 mol/L BQ aqueous solution, which can consume two times the amount of electrons needed for the complete reduction of Cr(VI) to Cr(III); **(c)** Photocatalytic reduction of aqueous Cr(VI) by PANI/SnS$_2$/NRG-2% and SnS$_2$ under visible-light (λ > 420 nm) irradiation with or without the addition of photogenerated electron scavenger (Potassium persulphate, KPS). *Note*: the dosage of KPS was 1 mL of 0.102 mol/L KPS aqueous solution, which can consume two times the amount of electrons needed for the complete reduction of Cr(VI) to Cr(III).

NRG-2% may contribute to its higher photocatalytic activity than SnS$_2$ nanoplates and SnS$_2$/PANI-7% in the reduction of aqueous Cr(VI) under the irradiation of visible-light (λ > 420 nm). According to the previous reports [17,19,20,24,26,29–32,36,39,44,71–74], the band gap (E$_g$) values of PANI, SnS$_2$ nanoplates, SnS$_2$/PANI-7% and PANI/SnS$_2$/NRG-2% were estimated on the basis of the theory concerning the optical absorption of direct band gap semiconductors (Eq. (4)):

$$\alpha h\nu = B(h\nu - E_g)^{1/2} \qquad (4)$$

where α, $h\nu$, and B denote in sequence absorption coefficient, energy of a photon with frequency ν, and a frequency-independent constant associated with the sample. The plots of $(\alpha h\nu)^2$ vs. $h\nu$ for PANI, SnS$_2$ nanoplates, SnS$_2$/PANI-7% and PANI/SnS$_2$/NRG-2% are shown in Fig. 7(b). Through extrapolating the straight-line portion of the $(\alpha h\nu)^2$ versus $h\nu$ plots to the abscissa axis, the E$_g$ values of PANI, SnS$_2$ nanoplates, SnS$_2$/PANI-7% and PANI/SnS$_2$/NRG-2% were determined to be 2.13, 2.15, 2.14 and 2.0 eV, respectively.
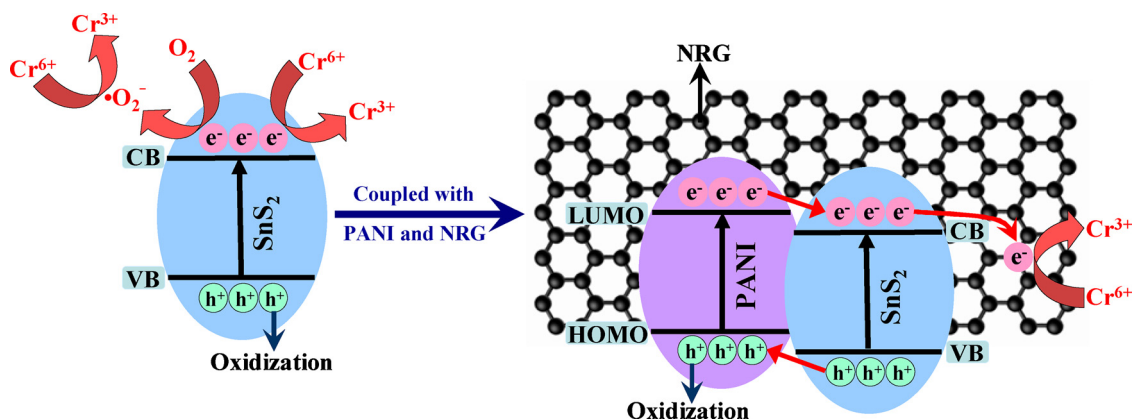
Fig. 8 shows the room temperature photoluminescence spectra of SnS$_2$ nanoplates, SnS$_2$/PANI-7% and PANI/SnS$_2$/NRG-2% upon 532 nm laser excitation. It can be observed from Fig. 8 that all the three samples displayed a photoluminescence peak around 541 nm, which may arise from the radiative recombination of the excitons of SnS$_2$ [9,26,37]. However, the photoluminescence peak intensities of SnS$_2$ nanoplates, SnS$_2$/PANI-7% and PANI/SnS$_2$/NRG-2% were in a descending order, suggesting that the separation rates of e^--h^+ pairs of SnS$_2$ nanoplates, SnS$_2$/PANI-7% and PANI/SnS$_2$/NRG-2% were in an ascending order [9,26,37]. Thus, it can be deduced that the coupling of SnS$_2$ with both PANI and NRG had synergistic effects in inhibiting the recombination of e^--h^+ pairs. The lower recombination rate of e^--h^+ pairs means that more e^- and h^+ are available to the photocatalytic reactions, making for higher photocatalytic efficiency (Fig. 2).

Fig. 9 shows the electrochemical impedance spectra of SnS$_2$ nanoplates, SnS$_2$/PANI-7% and PANI/SnS$_2$/NRG-2%. As can be seen from Fig. 9, the Nyquist arc radii of the three samples were in the order of SnS$_2$ nanoplates > SnS$_2$/PANI-7% > PANI/SnS$_2$/NRG-2%, suggesting that the interfacial charge transfer resistances of SnS$_2$ nanoplates, SnS$_2$/PANI-7% and PANI/SnS$_2$/NRG-2% were in a descending order [9,37]. Thus, the combination of SnS$_2$ with both PANI and NRG played synergistic roles in lowering the interfacial charge transfer resistance. This would favor the transfer and separation of e^- and h^+, contributing to increased photocatalytic efficiency [9,37].

Thus, it can be inferred from the above Fig. 7–9 that the coupling of SnS$_2$ with both PANI and NRG had synergistic effects in boosting the absorption of visible-light as well as the separation and transfer of e^- and h^+, which contributed to the significantly higher photocatalytic activity of PANI/SnS$_2$/NRG ternary composite. Besides, Fig. S4–S6 suggested that PANI/SnS$_2$/NRG-2% had the strongest absorption of visible-light and the highest efficiency in the separation and transfer of e^- and h^+, so contributing to its best photocatalytic performance.

3.4. Mechanisms of photocatalytic reduction of Cr(VI) by PANI/SnS$_2$/NRG composite and SnS$_2$

To probe the mechanisms of photocatalytic reduction of Cr(VI) by PANI/SnS$_2$/NRG-2% and SnS$_2$, the photocatalytic experiments were further conducted in N$_2$ atmosphere, as well as with the addition of superoxide anion radical (O$_2$·$^-$) scavenger (p-Benzoquinone, BQ) [27], and photogenerated electron (e^-) scavenger (Potassium persulphate, KPS) [75]. Fig. 10(a) indicated that the rate of photocatalytic reduction of Cr(VI) by SnS$_2$ in N$_2$ atmosphere was significantly retarded compared with that in air atmosphere, suggesting that O$_2$ played an important role in the photocatalytic reduction of Cr(VI) by SnS$_2$. By contrast, the rate of photocatalytic reduction of Cr(VI) by PANI/SnS$_2$/NRG-2% in N$_2$ atmosphere was only slightly slowed down compared with that in air atmosphere, suggesting that the influence of O$_2$ on the photocatalytic reduction of Cr(VI) by PANI/SnS$_2$/NRG-2% was slight. Fig. 10(b) showed that compared with the cases without BQ, the rate of SnS$_2$-mediated photocatalytic reduction of Cr(VI) became remarkably slower with the addition of BQ, whereas the rate of PANI/SnS$_2$/NRG-2%-mediated photocatalytic reduction of Cr(VI) was only slightly decelerated with the addition of BQ. Fig. 10(c) indicated that with the addition of KPS, the rate of photocatalytic reduction of Cr(VI) by SnS$_2$ did not decrease, whereas that by PANI/SnS$_2$/NRG-2% had an obvious

Scheme 1. Mechanisms of photocatalytic reduction of Cr(VI) by PANI/SnS$_2$/NRG composite and SnS$_2$.
Note: the reduction of Cr(VI) by O$_2\cdot^-$ also coexisted in the case of using PANI/SnS$_2$/NRG-2% as photocatalyst, but played only a relatively minor role. Hence, for highlighting the difference in the mechanisms of photocatalytic reduction of Cr(VI) by PANI/SnS$_2$/NRG composite and SnS$_2$, the reduction of Cr(VI) by O$_2\cdot^-$ in the case of using PANI/SnS$_2$/NRG-2% as photocatalyst is not shown in Scheme 1.
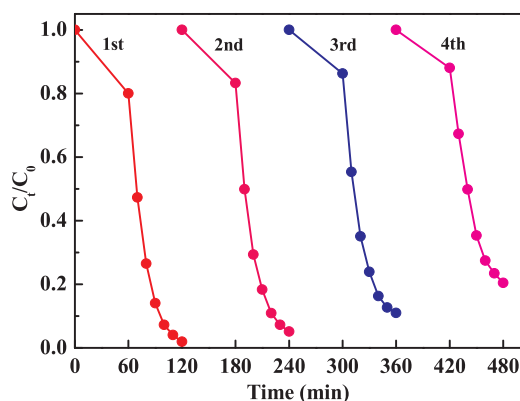

Fig. 11. Recycling performance of PANI/SnS$_2$/NRG-2% in photocatalytic reduction of aqueous Cr(VI) under the irradiation of visible-light (λ > 420 nm).

decrease. The above photocatalytic results suggested that SnS$_2$-mediated photocatalytic reduction of Cr(VI) was via two important pathways: (i) the reduction of Cr(VI) by e^- of SnS$_2$, because SnS$_2$ still maintained a large proportion of photocatalytic activity in the reduction of Cr(VI) in N$_2$ atmosphere; and (ii) the reduction by O$_2\cdot^-$, which came from the reduction of the adsorbed O$_2$ molecules by e^- of SnS$_2$. In contrast, PANI/SnS$_2$/NRG-2%-mediated photocatalytic reduction of Cr(VI) was dominantly through the reduction by e^-. However, the reduction of Cr(VI) by O$_2\cdot^-$ also coexisted in the case of using PANI/SnS$_2$/NRG-2% as photocatalyst, because the rate of PANI/SnS$_2$/NRG-2%-mediated photocatalytic reduction of Cr(VI) was also slightly lower in N$_2$ atmosphere or with the addition of BQ. Nonetheless, O$_2\cdot^-$ reduction played only a relatively minor role in the case of using PANI/SnS$_2$/NRG-2% as photocatalyst.

The potential of the valence band (VB) of SnS$_2$ nanoplates was determined to be about 1.07 V (vs. NHE) from their VB XPS spectrum in Fig. S7. The conduction band (CB) potential of SnS$_2$ nanoplates was calculated to be −1.08 V (vs. NHE), according to Equation (5):

$$E_{CB} = E_{VB} - E_g \tag{5}$$

The potential of the highest occupied molecular orbital (HOMO) of PANI was estimated to be + 0.58 V (vs. SCE) or 0.82 V (vs. NHE) from the oxidation potential in its cyclic voltammetry curve (Fig. S8). Accordingly, the lowest unoccupied molecular orbital (LUMO) potential of PANI was −1.31 V (vs. NHE), in consideration of that PANI had a E$_g$ of 2.13 eV. Hence, SnS$_2$ nanoplates and PANI had matched band structures for the formation of type-II heterojunction. Based on our current study and previous reports [34–37], the mechanisms of

photocatalytic reduction of Cr(VI) by PANI/SnS$_2$/NRG ternary composite and SnS$_2$ were proposed in Scheme 1. Under visible-light (λ > 420 nm) irradiation, both SnS$_2$ nanoplates and PANI were excited, producing e^- and h^+. Owing to the driving force of potential differences, the possible transfer of e^- was from PANI to SnS$_2$ to NRG, whereas the possible transfer of h^+ was from SnS$_2$ to PANI. Thus, compared with SnS$_2$, PANI/SnS$_2$/NRG ternary composite had dramatically increased separation rate of e^- and h^+, giving rise to more e^- and h^+ for the photocatalytic reactions. From the viewpoint of thermodynamics, the e^- in the CB of SnS$_2$ can reduce both O$_2$ to O$_2\cdot^-$ (Eϴ (O$_2$/O$_2\cdot^-$) = −0.33 V [27]) and Cr(VI) to Cr(III) (E^ϴ (Cr(VI)/Cr(V)) = + 0.55 V, E^ϴ (Cr(V)/Cr(IV)) = 1.34 V, and E^ϴ (Cr(IV)/Cr(III)) = 2.10 V [76]). Previous works have demonstrated that photocatalytic reduction of Cr(VI) to Cr(III) by semiconductors usually proceeds via three sequential one-electron transfer steps [76–79]. The first electron reduction (Cr(VI) + e_{CB}^- = Cr(V)) is the rate-determining step. Hence, if the CB potential of a semiconductor (such as SnS$_2$) is more negative than the reduction potential of Cr(VI)/Cr(V) couple, the reduction of Cr(VI) to Cr(III) by photogenerated electrons of the semiconductor would be feasible). In the absence of Cr(VI), the reduction of O$_2$ to O$_2\cdot^-$ by the e^- of both SnS$_2$ and PANI/SnS$_2$/NRG-2% would occur, as manifested by Fig. S9(a) and (b). This was consistent with the previous studies [26,27,32]. Nevertheless, Fig. S9(a) and (b) indicated that much more O$_2\cdot^-$ were generated by PANI/SnS$_2$/NRG-2% suspended in the mixed solvent of 1:1 dimethyl sulfoxide and water during the detection of O$_2\cdot^-$ using the DMPO ESR technique. This further manifested that PANI/SnS$_2$/NRG-2% was far superior to SnS$_2$ in the generation and separation of e^- and h^+. However, in the presence of Cr(VI), the reduction of Cr(VI) by e^- would be thermodynamically favorable and faster than the reduction of O$_2$ by e^- [76]. Moreover, the large Cr(VI) absorption capacity (about 20%) of PANI/SnS$_2$/NRG-2% also favored the reduction of Cr(VI) by e^- [80,81]. Hence, the photocatalytic reduction of Cr(VI) over PANI/SnS$_2$/NRG-2% was dominantly through the reduction by e^- (O$_2\cdot^-$ reduction played only a relatively minor role in the case of using PANI/SnS$_2$/NRG-2% as photocatalyst). In contrast, SnS$_2$ nanoplates had only a little adsorption of Cr(VI) (about 4%). Thus, the adsorbed O$_2$ molecules had increased access to capture e^- of SnS$_2$, resulting in more reduction of O$_2$ to O$_2\cdot^-$. Subsequently, O$_2\cdot^-$ also joined the reduction of Cr(VI) to Cr(III) [80,81]. Therefore, both e^- and O$_2\cdot^-$ reduction took important parts in SnS$_2$-mediated photocatalytic reduction of Cr(VI). It is worth mentioning that although many works have been devoted to developing SnS$_2$ and SnS$_2$-based composite photocatalysts for the reduction of aqueous Cr(VI) [22,23,33,54,59,82–86], none of them have experimentally investigated the underlying Cr(VI) reduction mechanisms. They just
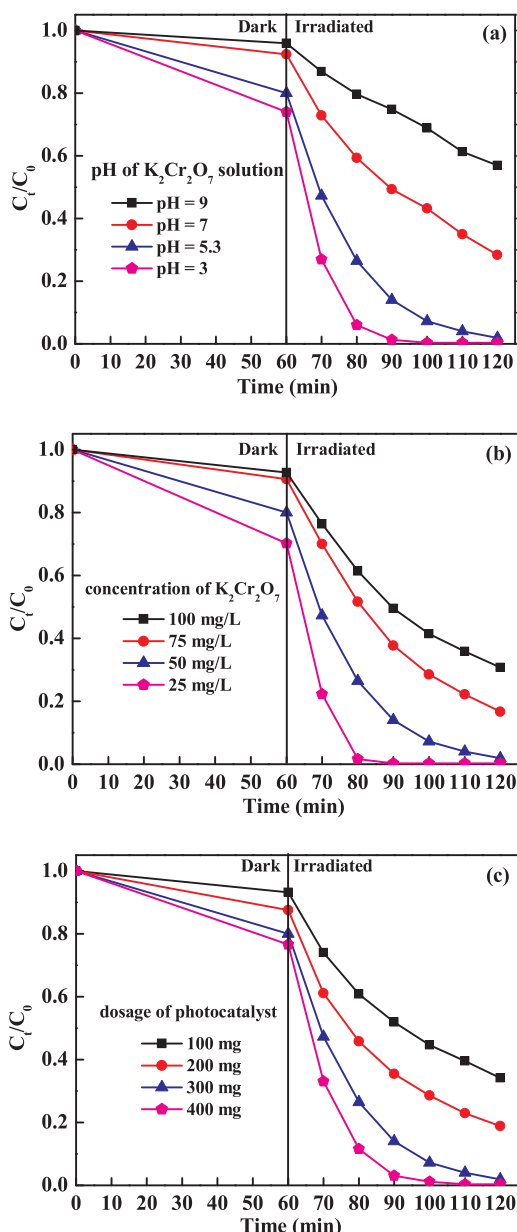
Fig. 12. Influences of (a) starting pH of Cr(VI) solution, (b) initial concentration of Cr(VI) solution, and (c) dosage of photocatalyst on the Cr(VI) removal rates by PANI/SnS$_2$/NRG-2%.

assumed that the photocatalytic reduction of Cr(VI) over SnS$_2$ and SnS$_2$-based composites was through the reduction of Cr(VI) by e^- [22,23,33,54,59,82–86]. However, their assumption should be inaccurate. Our current study revealed that both e^- and $O_2 \cdot^-$ reduction were responsible for SnS$_2$-mediated photocatalytic reduction of Cr(VI), whereas e^- reduction predominated the photocatalytic reduction of Cr(VI) over PANI/SnS$_2$/NRG-2% ($O_2 \cdot^-$ reduction played only a relatively minor role in the case of using PANI/SnS$_2$/NRG-2% as photocatalyst). These findings would be an important contribution to the scientific aspects of photocatalytic processes and basic understanding of SnS$_2$ and SnS$_2$-based composite photocatalysts as applied to the reduction of toxic Cr(VI).

3.5. Photocatalytic stability of PANI/SnS$_2$/NRG-2%

The photocatalytic stability of a new photocatalyst is also critical for practical applications. Hence, the recycling performance of PANI/SnS$_2$/

NRG-2% in photocatalytic reduction of aqueous Cr(VI) under the irradiation of visible-light ($\lambda > 420$ nm) was also examined. As shown in Fig. 11, the photocatalytic activity of PANI/SnS$_2$/NRG-2% did not exhibit sharp decline with the increase of reuse times, for example, near 80% of Cr(VI) can still be removed from the solution after 60 min visible-light ($\lambda > 420$ nm) irradiation during the fourth reuse of PANI/SnS$_2$/NRG-2%. This suggested that PANI/SnS$_2$/NRG-2% was stable and reusable for photocatalytic treatment of Cr(VI)-contaminated wastewaters.

3.6. Influence of photocatalytic testing parameters on the treatment of Cr(VI) by PANI/SnS$_2$/NRG-2%

It has been reported that the experimental conditions (such as starting pH and concentration of Cr(VI) solution, and dosage of photocatalyst) strongly influence the performance of a photocatalyst in treatment of Cr(VI) [1–7,16,35,82,86,87]. Moreover, optimization of the experimental conditions is very important for practical application of a new photocatalyst to treat Cr(VI)-polluted water. Therefore, in this study, the influences of the photocatalytic experimental conditions (including starting pH and concentration of Cr(VI) solution, and dosage of photocatalyst) on the efficiency of PANI/SnS$_2$/NRG-2% in removal of aqueous Cr(VI) were also investigated. From the results presented in Fig. 12(a–c), Fig. S10 (a–c) and Table 1, we can draw the following conclusions: lower starting pH and concentration of Cr(VI) solution, and larger dosage of photocatalyst can result in more efficient removal of Cr(VI) by PANI/SnS$_2$/NRG-2%. These results were consistent with the previous studies [1–7,16,35,82,86,87], and can also be rationalized by the underlying reasons as discussed in our earlier reports [86,87].

4. Conclusions

A new visible-light-activated ternary composite photocatalyst comprising SnS$_2$ nanoplates, PANI and NRG was synthesized via a three-step method. The PANI/SnS$_2$/NRG composite prepared under the optimized conditions (PANI/SnS$_2$/NRG-2%) exhibited remarkably higher photocatalytic activity than SnS$_2$ nanoplates, SnS$_2$/PANI and SnS$_2$/NRG binary composites in the reduction of aqueous Cr(VI) under the irradiation of visible-light ($\lambda > 420$ nm). The improved photocatalytic activity of PANI/SnS$_2$/NRG-2% was thought to be resulted from its increased absorption of visible-light and more efficient separation and transfer of photogenerated electrons and holes. Moreover, the photocatalytic reduction of Cr(VI) over PANI/SnS$_2$/NRG-2% was dominantly through the reduction by photogenerated electrons, whereas both photogenerated electron and superoxide anion radical ($O_2 \cdot^-$) reduction played important roles in SnS$_2$-mediated photocatalytic reduction of Cr(VI). Furthermore, lower initial pH and concentration of Cr(VI) solution, and larger dosage of photocatalyst can accelerate the photocatalytic treatment of Cr(VI) by PANI/SnS$_2$/NRG-2%.

Appendix A. Supplementary data

Supplementary material related to this article can be found, in the online version, at doi:https://doi.org/10.1016/j.apcatb.2018.05.002.

References

[1] Y. Li, W. Cui, L. Liu, R. Zong, Y. Zhu, Removal of Cr(VI) by 3D TiO$_2$-graphene hydrogel via adsorption enriched with photocatalytic reduction, Appl. Catal. B-

Environ. 199 (2016) 412–423.

[2] X. Wang, Y. Liang, W. An, J. Hu, Y. Zhu, W. Cui, Removal of chromium (VI) by a self-regenerating and metal free g-C3N4/graphene hydrogel system via the synergy of adsorption and photo-catalysis under visible light, Appl. Catal. B-Environ. 219 (2017) 53–62.

[3] L. Wang, C. Zhang, F. Gao, G. Mailhot, G. Pan, Algae decorated TiO2/Ag hybrid nanofiber membrane with enhanced photocatalytic activity for Cr(VI) removal under visible light, Chem. Eng. J. 314 (2017) 622–630.

[4] B.A. Marinho, R.O. Cristóvão, R. Djellabi, J.M. Loureiro, V.J.P. Vilar, Photocatalytic reduction of Cr(VI) over TiO2-coated cellulose acetate monolithic structures using solar light, Appl. Catal. B-Environ. 203 (2017) 18–30.

[5] F. Wang, X. Yi, C. Wang, J. Deng, Photocatalytic Cr(VI) reduction and organic-pollutant degradation in a stable 2D coordination polymer, Chin. J. Catal. 38 (2017) 2141–2149.

[6] F. Liu, J. Yu, G. Tu, L. Qu, J. Lei, J. Zhang, Carbon nitride coupled Ti-SBA15 catalyst for visible-light-driven photocatalytic reduction of Cr (VI) and the synergistic oxidation of phenol, Appl. Catal. B-Environ. 201 (2017) 1–11.

[7] G. Velegraki, J. Miao, C. Drivas, B. Liu, G.S. Armatas, Fabrication of 3D mesoporous networks of assembled CoO nanoparticles for efficient photocatalytic reduction of aqueous Cr(VI), Appl. Catal. B-Environ. 221 (2018) 635–644.

[8] C. Wang, X. Du, J. Li, X. Guo, Photocatalytic Cr(VI) reduction in metal-organic frameworks: a mini-review, Appl. Catal. B-Environ.193 (2016) 198–216.

[9] Y. Zhang, F. Zhang, Z. Yang, H. Xue, D.D. Dionysiou, Development of a new efficient visible-light-driven photocatalyst from SnS2 and polyvinyl chloride, J. Catal. 344 (2016) 692–700.

[10] S. Tonda, S. Kumar, M. Bhardwaj, P. Yadav, S. Ogale, g-C3N4/NiAl-LDH 2D/2D hybrid heterojunction for high-performance photocatalytic reduction of CO2 into renewable fuels, ACS Appl. Mater. Interfaces 10 (2018) 2667–2678.

[11] Z. Zhang, J. Huang, M. Zhang, Q. Yuan, B. Dong, Ultrathin hexagonal SnS2 nanosheets coupled with g-C3N4 nanosheets as 2D/2D heterojunction photocatalysts toward high photocatalytic activity, Appl. Catal. B-Environ. 163 (2015) 298–305.

[12] J. Lv, K. Dai, J. Zhang, Q. Liu, Facile constructing novel 2D porous g-C3N4/BiOBr hybrid with enhanced visible-light-driven photocatalytic activity, Sep. Purif. Technol. 178 (2017) 6–17.

[13] D. Jiang, T. Wang, Q. Xu, D. Li, M. Chen, Perovskite oxide ultrathin nanosheets/g-C3N4 2D-2D heterojunction photocatalysts with significantly enhanced photocatalytic activity towards the photodegradation of tetracycline, Appl. Catal. B-Environ. 201 (2017) 617–628.

[14] J. Wang, L. Tang, G. Zeng, Y. Deng, Atomic scale g-C3N4/Bi2WO6 2D/2D heterojunction with enhanced photocatalytic degradation of ibuprofen under visible light irradiation, Appl. Catal. B-Environ. 209 (2017) 285–294.

[15] Q. Wang, W. Wang, L. Zhong, D. Liu, F. Cui, Oxygen vacancy-rich 2D/2D BiOCl-g-C3N4 ultrathin heterostructure nanosheets for enhanced visible-light-driven photocatalytic activity in environmental remediation, Appl. Catal. B-Environ. 220 (2018) 290–302.

[16] J. Tu, X. Shi, H. Lu, Y. Yuan, Facile fabrication of SnS2 quantum dots for photoreduction of aqueous Cr(VI), Mater. Lett. 185 (2016) 303–306.

[17] J. Qu, D. Chen, N. Li, Q. Xu, J. Lu, Coral-inspired nanoscale design of porous SnS2 for photocatalytic reduction and removal of aqueous Cr (VI), Appl. Catal. B-Environ. 207 (2017) 404–411.

[18] X. Li, J. Zhu, H. Li, Comparative study on the mechanism in photocatalytic degradation of different-type organic dyes on SnS2 and CdS, Appl. Catal. B-Environ. 123–124 (2012) 174–181.

[19] S. Park, J. Park, R. Selvaraj, Y. Kim, Facile microwave-assisted synthesis of SnS2 nanoparticles for visible-light responsive photocatalyst, J. Ind. Eng. Chem. 31 (2015) 269–275.

[20] G. Liu, Y. Qiu, Z. Wang, J. Zhang, Z. Li, P. Hu, Efficiently synergistic hydrogen evolution realized by trace amount of Pt-decorated defect-rich SnS2 nanosheets, ACS Appl. Mater. Interfaces 9 (2017) 37750–37759.

[21] Y. Sun, G. Li, J. Xu, Z. Sun, Visible-light photocatalytic reduction of carbon dioxide over SnS2, Mater. Lett. 174 (2016) 238–241.

[22] X. Zhang, P. Zhang, L. Wang, H. Gao, Template-oriented synthesis of monodispersed SnS2@SnO2 hetero-nanoflowers for Cr(VI) photoreduction, Appl. Catal. B-Environ. 192 (2016) 17–25.

[23] J. Wang, X. Li, X. Li, J. Zhu, H. Li, Mesoporous yolk–shell SnS2–TiO2 visible photocatalysts with enhanced activity and durability in Cr(VI) reduction, Nanoscale 5 (2013) 1876–1881.

[24] T. Di, B. Zhu, B. Cheng, J. Yu, J. Xu, A direct Z-scheme g-C3N4/SnS2 photocatalyst with superior visible-light CO2 reduction performance, J. Catal. 352 (2017) 532–541.

[25] J. Chen, S. Liu, L. Zhang, N. Chen, New SnS2/La2Ti2O7 heterojunction photocatalyst with enhanced visible-light activity, Mater. Lett. 150 (2015) 44–47.

[26] X. Gao, G. Huang, H. Gao, C. Pan, H. Wang, J. Yan, Facile fabrication of Bi2S3/SnS2 heterojunction photocatalysts with efficient photocatalytic activity under visible light, J. Alloy. Compd. 674 (2016) 98–108.

[27] K. Yao, J. Li, S. Shan, Q. Jia, One-step synthesis of urchinlike SnS/SnS2 heterostructures with superior visible-light photocatalytic performance, Catal. Commun. 101 (2017) 51–56.

[28] J. Luo, X. Zhou, L. Ma, L. Xu, Enhancing visible light photocatalytic activity of direct Z-scheme SnS2/Ag3PO4 heterojunction photocatalysts, Mater. Res. Bull. 81 (2016) 16–26.

[29] J. Luo, X. Zhou, L. Ma, X. Xu, Enhanced photodegradation activity of methyl orange over Ag2CrO4/SnS2 composites under visible light irradiation, Mater. Res. Bull. 77 (2016) 291–299.

[30] C. Hou, Y. Zhang, J. Li, A. Zhu, In-situ hydrothermal synthesis of CeO2/SnS2 heterojunction for use as a new efficient visible-light-driven photocatalyst, Mater. Lett.

[31] Y. Liu, P. Geng, J. Wang, Z. Yang, H. Lu, J. Hai, In-situ ion-exchange synthesis Ag2S modified SnS2 nanosheets toward highly photocurrent response and photocatalytic activity, J. Colloid. Interf. Sci. 512 (2018) 784–791.

[32] F. Qiu, W. Li, F. Wang, H. Li, In-situ synthesis of novel Z-scheme SnS2/BiOBr photocatalysts with superior photocatalytic efficiency under visible light, J. Colloid Interf. Sci. 493 (2017) 1–9.

[33] Y. Zhong, X. Qiu, D. Chen, J. Lu, Flexible electrospun carbon nanofiber/tin(IV) sulfide core/sheath membranes for photocatalytically treating chromium(VI)-containing wastewater, ACS Appl. Mater. Interfaces 8 (2016) 28671–28677.

[34] H. Chauhan, K. Soni, M. Kumar, S. Deka, Tandem photocatalysis of graphene-stacked SnS2 nanodiscs and nanosheets with efficient carrier separation, ACS Omega 1 (2016) 127–137.

[35] Y. Yuan, D. Chen, X. Shi, J. Tu, Z. Zou, Facile fabrication of "green" SnS2 quantum dots/reduced graphene oxide composites with enhanced photocatalytic performance, Chem. Eng. J. 313 (2017) 1438–1446.

[36] P. Chen, Y. Su, H. Liu, Y. Wang, Interconnected tin disulfide nanosheets grown on graphene for Li-ion storage and photocatalytic applications, ACS Appl. Mater. Interfaces 5 (2013) 12073–12082.

[37] F. Zhang, T. Ding, Y. Zhang, Polyaniline modified SnS2 as a novel efficient visible-light-driven photocatalyst, Mater. Lett. 192 (2017) 149–152.

[38] X. Yuan, H. Wang, Y. Wu, X. Chen, M. Zeng, A novel SnS2–MgFe2O4/reduced graphene oxide flower-like photocatalyst: solvothermal synthesis, characterization and improved visible-light photocatalytic activity, Catal. Commun. 61 (2015) 62–66.

[39] F. Deng, X. Lu, X. Pei, X. Lu, O, fabrication of ternary reduced graphene oxide/SnS2/ZnFe2O4 composite for high visible-light photocatalytic activity and stability, J. Hazard. Mater. 332 (2017) 149–161.

[40] J. Yang, D. Chen, Y. Zhu, Y. Zhang, Y. Zhu, 3D-3D porous Bi2WO6/graphene hydrogel composite with excellent synergistic effect of adsorption-enrichment and photocatalytic degradation, Appl. Catal. B-Environ. 205 (2017) 228–237.

[41] X. Bai, C. Sun, D. Liu, X. Luo, Y. Zhu, Photocatalytic degradation of deoxynivalenol using graphene/ZnO hybrids in aqueous suspension, Appl. Catal. B-Environ. 204 (2017) 11–20.

[42] H. Zhang, Y. Zhu, Significant visible photoactivity and antiphotocorrosion performance of CdS photocatalysts after monolayer polyaniline hybridization, J. Phys. Chem. C 114 (2010) 5822–5826.

[43] H. Zhang, R. Zong, Y. Zhu, Photocorrosion inhibition and photoactivity enhancement for zinc oxide via hybridization with monolayer polyaniline, J. Phys. Chem. C 113 (2009) 4605–4611.

[44] C. Wang, L. Wang, J. Jin, J. Liu, B. Su, Probing effective photocorrosion inhibition and highly improved photocatalytic hydrogen production on monodisperse PANI@CdS core-shell nanospheres, Appl. Catal. B-Environ. 188 (2016) 351–359.

[45] L. Liu, L. Ding, Y. Liu, W. An, W. Cui, A stable Ag3PO4@PANI core@shell hybrid: enrichment photocatalytic degradation with π-π conjugation, Appl. Catal. B-Environ. 201 (2017) 92–104.

[46] X. Chen, H. Li, J. Pan, X. Xiong, Fabrication of TiO2@PANI nanobelts with the enhanced absorption and photocatalytic performance under visible light, Mater. Lett. 172 (2016) 52–55.

[47] W. Cui, J. He, H. Wang, J. Hu, Y. Liang, Polyaniline hybridization promotes photo-electro-catalytic removal of organic contaminants over 3D network structure of rGH-PANI/TiO2 hydrogel, Appl. Catal. B-Environ. 232 (2018) 232–245.

[48] H. Yu, X. Huang, J. Yu, Enhanced photoinduced-stability and photocatalytic activity of CdS by dual amorphous cocatalysts: synergistic effect of Ti(IV)-hole cocatalyst and Ni(II)-electron cocatalyst, J. Phys. Chem. C 120 (2016) 3722–3730.

[49] J. Miao, A. Xie, S. Li, F. Huang, Y. Shen, A novel reducing graphene/polyaniline/cuprous oxide composite hydrogel with unexpected photocatalytic activity for the degradation of Congo red, Appl. Surf. Sci. 360 (2016) 594–600.

[50] A.P. Gaikwad, D. Tyagi, C.A. Betty, R. Sasikala, Photocatalytic and photo electrochemical properties of cadmium zinc sulfide solid solution in the presence of Pt and RuS2 dual co-catalysts, Appl. Catal. A-Gen. 517 (2016) 91–99.

[51] L. Zhang, Y. Shi, L. Wang, C. Hu, AgBr-wrapped Ag chelated on nitrogen-doped reduced graphene oxide for water purification under visible light, Appl. Catal. B-Environ. 220 (2018) 118–125.

[52] Z. Yue, A. Liu, C. Zhang, J. Huang, M. Zhu, P. Yang, Noble-metal-free heterostructural CdS/Nb2O5/N-doped-graphene ternary photocatalytic system as visible-light-driven photocatalyst for hydrogen evolution, Appl. Catal. B-Environ. 201 (2017) 202–210.

[53] Q. Guo, H. Li, Q. Zhang, Y. Zhang, Fabrication, characterization and mechanism of a novel Z-scheme Ag3PO4/NG/polyimide composite photocatalyst for microcystin-LR degradation, Appl. Catal. B-Environ. 229 (2018) 192–203.

[54] Y. Yang, X. Yang, D. Leng, S. Wang, W. Zhang, Fabrication of g-C3N4/SnS2/SnO2 nanocomposites for promoting photocatalytic reduction of aqueous Cr(VI) under visible light, Chem. Eng. J. 335 (2018) 491–500.

[55] X. Yang, Y. Xiang, Y. Qu, X. Ding, Novel in situ fabrication of conjugated microporous poly(benzothiadiazole)–Bi2MoO6 Z-scheme heterojunction with enhanced visible light photocatalytic activity, J. Catal. 345 (2017) 319–328.

[56] Y. Zhang, M. Xu, H. Li, H. Ge, Z. Bian, The enhanced photoreduction of Cr(VI) to Cr (III) using carbon dots coupled TiO2 mesocrystals, Appl. Catal. B-Environ. 226 (2018) 213–219.

[57] D. Lu, W. Chai, M. Yang, P. Fang, Visible light induced photocatalytic removal of Cr (VI) over TiO2-based nanosheets loaded with surface-enriched CoOx nanoparticles and its synergism with phenol oxidation, Appl. Catal. B-Environ. 190 (2016) 44–65.

[58] J. Yu, C. Xu, F. Ma, S. Hu, L. Zhen, Monodisperse SnS2 nanosheets for high-performance photocatalytic hydrogen generation, ACS Appl. Mater. Interfaces 6 (2014) 22370–22377.

[59] Y.C. Zhang, L. Yao, G. Zhang, D.D. Dionysiou, One-step hydrothermal synthesis of

high-performance visible-light-driven SnS$_2$/SnO$_2$ nanoheterojunction photocatalyst for the reduction of aqueous Cr(VI), Appl. Catal. B-Environ. 144 (2014) 730–738.

[60] J.F. Moulder, W.F. Stickle, P.E. Sobol, K.D. Bomben, J. Chastain (Ed.), Handbook of X-ray Photoelectron Spectroscopy, Perkin-Elmer Corporation, Eden Prairie, 1992.

[61] L. Yang, J. Hu, L. He, J. Tang, Y. Zhou, J. Li, One-pot synthesis of multifunctional magnetic N-doped graphene composite for SERS detection, adsorption separation and photocatalytic degradation of Rhodamine 6G, Chem. Eng. J. 327 (2017) 694–704.

[62] Y. Xu, Y. Mo, J. Tian, P. Wang, H. Yu, J. Yu, The synergistic effect of graphitic N and pyrrolic N for the enhanced photocatalytic performance of nitrogen-doped graphene/TiO$_2$ nanocomposites, Appl. Catal. B-Environ. 181 (2016) 810–817.

[63] Q. Liang, H. Luo, J. Geng, Facile one-pot preparation of nitrogen-doped ultra-light graphene oxide aerogel and its prominent adsorption performance of Cr(VI), Chem. Eng. J. 338 (2018) 62–71.

[64] T.D. Pham, B.K. Lee, V.N. Nguyen, Novel photocatalytic activity of vanadium-doped tantalum nitride sensitized/protected by polyaniline for efficient visible light water splitting, J. Catal. 352 (2017) 13–21.

[65] Y. Gao, C. Chen, X. Tan, Polyaniline-modified 3D-flower-like molybdenum disulfide composite for efficient adsorption/photocatalytic reduction of Cr(VI), J. Colloid Interf. Sci. 476 (2016) 62–70.

[66] J. Feng, Y. Hou, X. Wang, L. Li, In-depth study on adsorption and photocatalytic performance of novel reduced graphene oxide-ZnFe$_2$O$_4$-polyaniline composites, J. Alloy. Compd. 681 (2016) 157–166.

[67] W. Zhang, H. Guo, H. Sun, R. Zeng, Constructing ternary polyaniline-graphene-TiO$_2$ hybrids with enhanced photoelectrochemical performance in photo-generated cathodic protection, Appl. Surf. Sci. 410 (2017) 547–556.

[68] X. Yuan, Y. Xu, H. Meng, X. Zhang, Fabrication of ternary polyaniline-graphene oxide-TiO$_2$ hybrid films with enhanced activity for photoelectrocatalytic hydrogen production, Sep. Purif. Technol. 193 (2018) 358–367.

[69] H. Wu, S. Lin, C. Chen, W. Liang, H. Yang, A new ZnO/rGO/polyaniline ternary nanocomposite as photocatalyst with improved photocatalytic activity, Mater. Res. Bull. 83 (2016) 434–441.

[70] G. Ma, Y. Chen, L. Li, An attractive photocatalytic inorganic antibacterial agent: preparation and property of graphene/zinc ferrite/polyaniline composites, Mater. Lett. 131 (2014) 38–41.

[71] Y.C. Zhang, J. Li, M. Zhang, D.D. Dionysiou, Size-tunable hydrothermal synthesis of SnS$_2$ nanocrystals with high performance in visible light-driven photocatalytic reduction of aqueous Cr(VI), Environ. Sci. Technol. 45 (2011) 9324–9331.

[72] H. Wei, C. Hou, Y. Zhang, Z. Nan, Scalable low temperature in air solid phase synthesis of porous flower-like hierarchical nanostructure SnS$_2$ with superior performance in the adsorption and photocatalytic reduction of aqueous Cr(VI), Sep. Purif. Technol. 189 (2017) 153–161.

[73] R. Wei, J. Hu, T. Zhou, Ultrathin SnS$_2$ nanosheets with exposed {001} facets and enhanced photocatalytic properties, Acta Mater. 66 (2014) 163–171.

[74] M.J. Almasi, T. Fanaei Sheikholeslami, M.R. Naghdi, Band gap study of polyaniline and polyaniline/MWNT nanocomposites with in situ polymerization method, Compos. Part B-Eng. 96 (2016) 63–68.

[75] C. Wang, J. Li, X. Lv, Y. Zhang, G. Guo, Photocatalytic organic pollutants degradation in metal-organic frameworks, Energy Environ. Sci. 7 (2014) 2831–2867.

[76] M.I. Litter, Last advances on TiO$_2$-photocatalytic removal of chromium, uranium and arsenic, Curr. Opin. Green Sustain. Chem. 6 (2017) 150–158.

[77] J.J. Testa, M.A. Grela, M.I. Litter, Experimental evidence in favor of an initial one-electron-transfer process in the heterogeneous photocatalytic reduction of chromium(VI) over TiO$_2$, Langmuir 17 (2001) 3515–3517.

[78] J.M. Meichtry, M. Brusa, G. Mailhot, M.A. Grela, M.I. Litter, Heterogeneous photocatalysis of Cr(VI) in the presence of citric acid over TiO$_2$ particles: relevance of Cr(V)–citrate complexes, Appl. Catal. B-Environ. 71 (2007) 101–107.

[79] A.E. Giannakas, E. Seristatidou, Y. Deligiannakis, I. Konstantinou, Photocatalytic activity of N-doped and N–F co-doped TiO$_2$ and reduction of chromium(VI) in aqueous solution: an EPR study, Appl. Catal. B-Environ. 132–133 (2013) 460–468.

[80] G. Dong, L. Zhang, Synthesis and enhanced Cr(VI) photoreduction property of formate anion containing graphitic carbon nitride, J. Phys. Chem. C 117 (2013) 4062–4068.

[81] H. Wei, Q. Zhang, Y. Zhang, D.D. Dionysiou, Enhancement of the Cr(VI) adsorption and photocatalytic reduction activity of g-C$_3$N$_4$ by hydrothermal treatment in HNO$_3$ aqueous solution, Appl. Catal. A-Gen. 521 (2016) 9–18.

[82] C. Mondal, M. Ganguly, J. Pal, A. Roy, J. Jana, T. Pal, Morphology controlled synthesis of SnS$_2$ nanomaterial for promoting photocatalytic reduction of aqueous Cr(VI) under visible light, Langmuir 30 (2014) 4157–4164.

[83] Y.C. Zhang, J. Li, H.Y. Xu, One-step in-situ solvothermal synthesis of SnS$_2$/TiO$_2$ nanocomposites with high performance in visible light-driven photocatalytic reduction of aqueous Cr(VI), Appl. Catal. B-Environ. 123–124 (2012) 18–26.

[84] L. Ma, L. Xu, X. Xu, L. Zhang, X. Zhou, Fabrication of SnO$_2$/SnS$_2$ hybrids by anchoring ultrafine SnO$_2$ nanocrystals on SnS$_2$ nanosheets and their photocatalytic properties, Ceram. Int. 42 (2016) 5068–5074.

[85] M. Sun, Q. Yan, T. Yan, B. Du, Facile fabrication of 3D flower-like heterostructured g-C$_3$N4/SnS$_2$ composite with efficient photocatalytic activity under visible light, RSC Adv. 4 (2014) 31019–31027.

[86] F. Zhang, Y. Zhang, C. Zhou, Z. Yang, D.D. Dionysiou, A new high efficiency visible-light photocatalyst made of SnS$_2$ and conjugated derivative of polyvinyl alcohol and its application to Cr(VI) reduction, Chem. Eng. J. 324 (2017) 140–153.

[87] J. Li, T. Peng, Y. Zhang, C. Zhou, A. Zhu, Polyaniline modified SnO$_2$ nanoparticles for efficient photocatalytic reduction of aqueous Cr(VI) under visible light, Sep. Purif. Technol. 201 (2018) 120–129.